

Nanowire growth and sublimation: CdTe quantum dots in ZnTe nanowires

M. Orrù,^{1,2} E. Robin,² M. Den Hertog,¹ K. Moratis,¹ Y. Genuist,¹
R. André,¹ D. Ferrand,¹ J. Cibert,^{1,*} and E. Bellet-Amalric²

¹*Univ. Grenoble Alpes, CNRS, Institut NEEL, F-38000 Grenoble, France*

²*Univ. Grenoble Alpes, CEA, INAC, F-38000 Grenoble, France*

(Dated: August 7, 2018)

The role of the sublimation of the compound and of the evaporation of the constituents from the gold nanoparticle during the growth of semiconductor nanowires is exemplified with CdTe-ZnTe heterostructures. Operating close to the upper temperature limit strongly reduces the amount of Cd present in the gold nanoparticle and the density of adatoms on the nanowire sidewalls. As a result, the growth rate is small and strongly temperature dependent, but a good control of the growth conditions allows the incorporation of quantum dots in nanowires with sharp interfaces and adjustable shape, and it minimizes the radial growth and the subsequent formation of additional CdTe clusters on the nanowire sidewalls, as confirmed by photoluminescence. Uncapped CdTe segments dissolve into the gold nanoparticle when interrupting the flux, giving rise to a bulb-like (pendant-droplet) shape attributed to the Kirkendall effect.

Keywords: energy dispersive x-ray spectrometry, nanowires, core-shell nanowires, quantum dots, electron microscopy, photoluminescence, Kirkendall effect

I. INTRODUCTION

Fabricating semiconductor quantum dots (QD) embedded in a nanowire (NW) constitutes a more flexible process than the usual Stranski-Krastanow growth mode: it permits to combine various materials with various strain configurations, and adjustable shape and size. One interest of adjusting the aspect ratio and the strain configuration [1, 2] is that it allows one to shape the hole state ("heavy hole" or "light hole"), without involving complex structures[3]. This has a strong impact on the optical selection rules: emission diagram for classical photonic devices, photovoltaics, and quantum devices for optical manipulation of the electron or hole state in a doped quantum dot - these aspects are particularly attractive for III-V and II-VI material combinations. It also governs the spin properties.

The growth of NWs by molecular beam epitaxy (MBE) is generally achieved thanks to a nano-sized catalyst, most often a gold droplet (the so-called vapor-liquid-solid growth mode, or VLS): the elements constituting the NW are trapped in the droplet where the nucleation to form the semiconductor is more efficient than in the neighboring vapor phase. The QD is inserted by switching the impinging flux for a certain time, which controls the QD height, while the diameter of the contact area between the catalyst and the NW controls the diameter of the QD. For a good control of the QD shape, sharp interfaces are needed, meaning that the problem of "reservoir effect" (the progressive change of composition of the droplet when switching the flux) has to be circumvented. Various solutions were proposed. Silicon-germanium axial heterostructures were fabricated using a solid catalyst instead of a liquid one (vapor-solid-solid growth, or VSS,

instead of VLS): the solubility is expected to be lower [4] and a model was proposed which assumes that surface and interface diffusion takes place instead of diffusion through the catalyst nanoparticle [5]. In III-V heterostructures, the reservoir effect is small, a few %, when dealing with column-V atoms [6, 7] but the residual pressure in the MBE chamber has to be mastered. The reservoir effect is more severe when dealing with column-III atoms, and elaborate sequences were designed to make it as small as possible [8, 9].

We address the growth of QDs embedded in NWs made of II-VI semiconductors. Several aspects make such structures particularly attractive. Light-hole emission was reported in such CdTe QDs in ZnTe NWs [10]. Single photon emission was observed up to room temperature in CdSe QDs in ZnSe NWs [11]. II-VI QDs in NWs can incorporate a dilute magnetic semiconductor[12]: in that case one can expect the formation of a magnetic polaron around a hole trapped in the QD, which constitutes a model system for ultimate magnetic objects where the superparamagnetic state is induced by one or a small number of carriers, so that it can be controlled by a low applied bias. Again, the anisotropy is governed by the hole state - a feature reminiscent of carrier induced ferromagnetism in a quantum well. Finally, CdTe NWs have been used recently [13] as a template for the growth of HgTe NWs in the quest for 1D topological insulators.

It has been recognized for some time that the growth window for CdTe NWs, using MBE with a gold catalyst, is extremely narrow, with a high temperature limit attributed to the sublimation of CdTe [14]. Indeed a dramatic drop of the growth rate is observed when the temperature is increased by a few degrees above 350°C. Our goal here is to make this observation more quantitative and to unravel the role played in the growth of CdTe by the sublimation of CdTe and the evaporation of Cd from the gold catalyst, and the consequences for the

* joel.cibert@neel.cnrs.fr

properties of CdTe QDs.

II. EXPERIMENTAL METHODS AND SAMPLES

A. Growth by molecular beam epitaxy

The details of the conditions used for the sample preparation and the growth of NWs have been reported previously [15]. The growth was achieved by MBE in a Riber 32 chamber, using solid catalyst particles formed by dewetting a fraction of a monolayer of gold deposited on a ZnTe buffer on a GaAs substrate. All fluxes were calibrated prior to growth by measuring the RHEED oscillations on a ZnTe or CdTe (001) test substrate: for instance the Zn flux (and the Te flux) from the ZnTe cell is measured by the growth rate of a ZnTe layer, in ML s^{-1} , with an additional Zn flux from a Zn cell [16]. The sample holder was aligned on the horizontal line containing the CdTe cell (angle of incidence α in the horizontal plane, $\tan \alpha = 0.21$) while our ZnTe cell is on the other cell line ($\tan \alpha = 0.48$).

B. EDX and TEM

We used energy dispersive x-ray (EDX) spectrometry coupled to a FEI Tecnai Osiris scanning transmission electron microscope (TEM) equipped with four Silicon Drift Detectors and operated at 200 kV. The NWs were removed mechanically from the as-grown samples and deposited on a holey carbon-coated copper grid. The EDX signal is an hypermap where each pixel corresponds to the x-ray emission of atoms along the electron beam path. We used the QUANTAX-800 software from Bruker for background correction and deconvolution to extract the contributions of the L lines of Te, Cd, Au, and K lines of Zn and O. The absorption correction - for the typical size of the NWs - was estimated to be negligible for Te, Zn, Cd and less than 10% for O. The cross-sections for each element are deduced from the so-called ζ -factors directly measured on our equipment at the same operating conditions using reference samples of known composition and thickness [17].

High angle annular dark field (HAADF) high resolution scanning TEM images were realized on a probe corrected FEI Titan Themis operated at 200 kV.

C. Samples

In this paper we discuss three samples grown by MBE on a ZnTe buffer layer, in the VSS mode. They incorporate a series of CdTe-based insertions, see Fig. 1a, in a micrometer-long ZnTe NW: sample I to test the CdTe-ZnTe interfaces, sample T to test the effect of growth

temperature, and sample R to measure the growth rate by testing the effect of the duration of the CdTe pulse.

The three samples are:

- Sample I (interfaces) contains a series of thin CdTe insertions which were previously used as markers to follow the growth of the ZnTe NW [15]; the intended structure of this sample is shown schematically at the top of Fig. 1a.
- Sample T (temperature) involves a series of CdTe pulses of identical duration, but the temperature was decreased by steps of 5°C at the middle of each ZnTe sequence, down to 350°C for the last insertion.
- Sample R (rate) was designed to measure the growth rate by testing the effect of the duration of the CdTe pulse: the duration was increased by a factor 2 for each insertion; the nominal growth temperature was 375°C .

The last sequence was ZnTe for sample I and CdTe for sample T and R. The position of the insertions along the NW is such that the growth of the CdTe insertion and of the surrounding shells is essentially due to the flux impinging onto the catalyst and onto the sidewalls of the NW, with no contribution of adatoms diffusing from the substrate [15]. In all cases we observe both zincblende NWs, with a cone shape, and wurtzite NWs, with a cylinder shape [18]. The local composition has been determined by a quantitative modeling [19] of EDX spectrometry, and by the geometrical phase analysis (GPA) [20, 21] of TEM images.

Section III describes the experimental results obtained on these three samples. Based on these results, section IV proposes a modified version of the model previously used to describe the growth of ZnTe NWs [15]: we incorporate the sublimation of CdTe and the evaporation of Cd from the gold nanoparticle. Finally section V discusses the consequences for the axial and radial growth rates and the influence on the luminescence properties of a CdTe dot in ZnTe NW; it also describes the impact on the nanoparticle, which acquires a bulb-like shape which we attribute to the Kirkendall effect induced by a redissolution of CdTe.

III. EXPERIMENTAL RESULTS

Figure 1 displays the result of the EDX study of one NW from sample I. The profile (Fig. 1e) is not symmetrical and features a tail towards the NW tip; the Cd content x of $\text{Cd}_x\text{Zn}_{1-x}\text{Te}$ at position z can be fitted with two interfaces separated by a distance d , $x(z) = x_i(z - d/2) - x_i(z + d/2)$, each interface being broadened by a Gaussian of width σ and an exponential of length τ extending along the growth direction towards the tip. While a more sophisticated model of the interface could be elaborated [6, 9], as suggested by the different growth

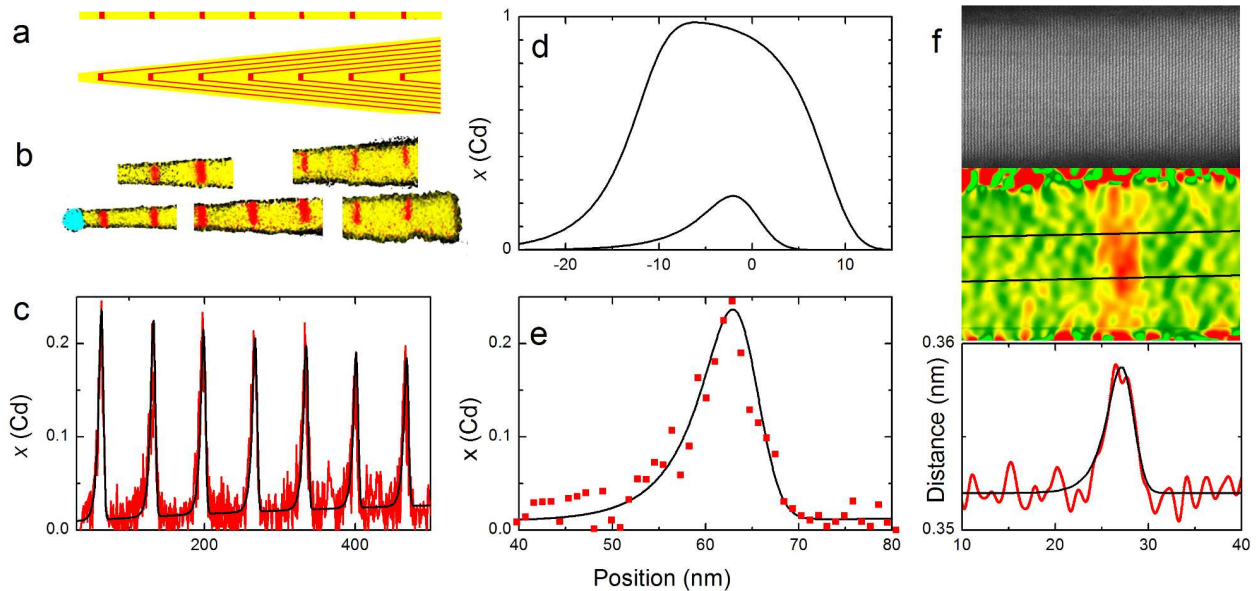


FIG. 1. Sample I: (a) scheme of the structure of the NW without (top) and with (bottom) radial growth; (b) EDX map along one NW, showing the area where O (black), Au (cyan), Cd (red) and Zn (yellow) exceed an arbitrary concentration; (c) EDX axial profile of Cd in the same NW, with fit; (d) two examples of the fitting profile obtained using Eq. 1, one with an insertion length as in (e) and another one with a 10 times longer insertion; (e) EDX profile of the topmost insertion in (c), and fit with Eq. 1, $d = 2$ nm, $\tau = 4$ nm, $\sigma = 2$ nm; (f) TEM image (top) and GPA profile (bottom) averaged on the band indicated in the image); the fit uses $d = 1.4$ nm, $\tau = 1.5$ nm, $\sigma = 1$ nm.

rates of CdTe and ZnTe and the different values of their formation energy, it would require an accurate knowledge of the thermodynamics of Cd, Zn and Te in the gold nanoparticle and this is beyond the scope of the present study. Going on with the simple hypothesis of an exponential tail, the convoluted profile is obtained by a straightforward calculation as

$$x_i(z) = \frac{1}{2} \left[1 - \operatorname{erf}\left(\frac{z}{\sqrt{2}\sigma}\right) \right] + \frac{1}{2} \left[1 + \operatorname{erf}\left(\frac{z - \sigma^2/\tau}{\sqrt{2}\sigma}\right) \right] \exp\left(-\frac{z - \sigma^2/2\tau}{\tau}\right) \quad (1)$$

Figure 1d shows two examples of such a profile, the one which provides a good fit to the measured EDX profile (Fig. 1e), and the other one with a ten-times thicker insertion, which allows a better identification of the role of the exponential tails.

Finally, Fig. 1c and 1e show that the same individual profile, with the same parameters, well describes the overall axial profile of the NW, provided we take into account the presence of the radial ZnTe-CdTe multishell structure, as schematized in the bottom part of Fig. 1a. This multishell structure is due to lateral growth: for instance, during the growth of a CdTe insertion, Cd adatoms which are present on the NW sidewalls and do not reach the gold nanoparticle may induce some lateral growth of CdTe and form a CdTe shell over the previously

grown sections of the NW; of course this shell will be absent from the sections grown subsequently. In a symmetrical way, a ZnTe shell is formed during the growth of each ZnTe section. The resulting structure, with an increasing number of individual shells from the NW tip to its base, is schematically displayed at the bottom of Fig. 1a, where the lateral growth has been exaggerated. The EDX analysis provides the average Cd content (with respect to Cd+Zn) averaged over the electron beam path. The presence of Zn shells creates the tapering and this additional Zn content along the electron beam path decreases the signal measured at each insertion in Fig. 1c; the fit assumes a factor of 1.6 between the diameter along the electron beam path at the basis and at the tip of the NW. The presence of Cd shells slightly contributes to the tapering, and creates the rising background between the insertions in Fig. 1c: the fit assumes that a CdTe shell of thickness ~ 0.2 nm (half a monolayer) is added by the growth of each insertion.

This NW from sample I had been transferred onto a grid for the EDX study and it may have been broken during the harvesting process. Other NWs were observed by TEM on a cleaved edge [15] so that we are sure that they grew perpendicular to the substrate, and that they are complete although their basis is hidden by the 2D layer grown at the same time as the NWs. Profiles were obtained by GPA: GPA measures the crystal plane distance, also averaged over the electron beam path, with respect to its value measured in the ZnTe sequence. An example

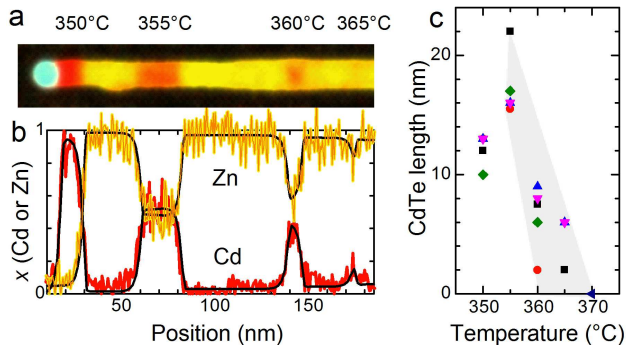


FIG. 2. Sample T: (a) EDX map (cyan: Au; yellow: Zn; red: Cd) and TEM image of a NW (scale bar 20 nm); (b) axial profile of Cd and Zn concentrations in the same NW, with fit (black solid lines) using the same interface profile $\tau = 2.0$ nm, $\sigma = 0.5$ nm and different values of length d ; (c) length d of the CdTe insertions measured on several NWs, as a function of growth temperature; the grey area suggests the trend followed by the capped insertions, while the uncapped ones are shorter.

is displayed in Fig. 1f. A good fit of the experimental profile is obtained with slightly lower values of the parameters, d and $\tau \approx 1.5$ nm and $\sigma \approx 1$ nm. The larger values of the parameters measured by EDX are probably partly of instrumental origin (GPA requires a perfect alignment of the NW in the TEM, EDX does not); they may be due also to a slight angle of the NW axis with respect to the substrate normal during the growth: notice the rather strong tapering, and the asymmetric shell surrounding the CdTe insertions. We conclude that this kind of profile is validated by EDX and GPA, and it will be used in the following.

Figure 2 displays the results of the EDX study of a NW from sample T, with CdTe insertions grown at different temperatures: TEM image, EDX map, axial EDX profiles for Cd and Zn (total=1), and its fit with Eq. 1, $\tau = 2.0$ nm, $\sigma = 0.5$ nm and different values of d . The CdTe pulse was the same for all insertions, about 4 times larger than in sample I. It is clear that the CdTe dot grown at 355°C is much longer than the dot at 360°, while the dot at 365° almost disappeared. This trend was confirmed on 6 other NWs from sample T, with either wurtzite or zinc-blende structure, with the results gathered in Fig. 2c. Two additional NWs in the series are long enough to confirm that dots grown at 370°C are beyond the detection limit by EDX.

Figure 3 displays the results obtained on sample R, where the length of the CdTe pulse was progressively increased. The EDX map (Fig. 3a) indeed suggests that the length of the CdTe insertion correspondingly increases, but for the last, uncapped insertion. The axial profile (Fig. 3b) and the plot in Fig. 3c confirm the length-duration dependance.

The radial profiles (Fig. 3d) reveal interesting features. Summing all contributions, we can plot the local thickness of the NW, which is best fitted assuming an hexago-

nal cross section. In the analysis[19], the fitting parameters are the overall orientation of the facets with respect to the electron beam (the vertical axis in the schemes of Fig. 3d, which was not oriented with respect to the crystal structure in the NW) and the distance between opposite facets. Profile d(2) reveals a ZnTe core with a shell enriched in CdTe; the thickness of the shell is difficult to ascertain, but the total amount of CdTe corresponds to less than a monolayer of pure CdTe. Profile d(1) points to an almost pure CdTe core with a thin shell enriched in ZnTe. Profile d(3) demonstrates an increase of the thickness by lateral overgrowth (tapering), with a ZnTe-rich shell; the apparent Cd content of the core is reduced, part of it is due to the presence of the thicker ZnTe shell, but we cannot exclude some radial diffusion of Cd from the core to the shell. Note that all inter-facet distances increase from d(1) to d(2) and d(2) to d(3), but not identically, so that the shape of the hexagons is changed ($\pm 10\%$ with respect to the regular hexagon). Although we have no definitive interpretation, we have already noted [15] that the shape of the nanoparticle is affected by random changes during the growth. This affects both radial and axial growth (and it probably accounts for a part of the length fluctuations observed in Fig. 2c and Fig. 3c). It does not invalidate the general conclusion of the present study.

The temperature dependance of the CdTe growth rate, as demonstrated in Fig. 2c, is completely different from the weak temperature dependance that we found for ZnTe [15]. In the following we show that this difference is due for a part to the cell-NW geometry, and for the greatest part to the evaporation of Cd from the nanoparticle and the sublimation of CdTe from the sidewalls, which are both significant in this temperature range when compared to the impinging flux.

IV. MODEL

Elaborating on the model previously used to describe the growth of ZnTe NWs [15], we consider a NW with a quasi-sphere nanoparticle of diameter D_{NP} . The NW diameter at the tip, noted D_{NW} , may be different: in the case of ZnTe, our previous analysis of the growth rate [15] lead us to assume $D_{NW}/D_{NP} \approx 0.6$. In the case of CdTe, we will keep the same values as a reasonable starting point. The normal component of the incident flux, J_s , has been measured from RHEED (reflexion high energy electron diffraction) oscillations during growth on a test substrate; it is expressed as the growth rate of a 2D layer, in nm s^{-1} . The NW is normal to the substrate and the angle of incidence of the flux is α : in our MBE chamber, $\tan \alpha = 0.21$ for the CdTe cell and 0.48 for the ZnTe cell. The NW length is significantly larger than the diffusion length along the sidewalls ($\lambda \approx 80$ nm at 350°C for ZnTe [15]), so that the diffusion of adatoms from the substrate is negligible. Hence there are two contributions to the NW growth: (1) the direct flux to the nanoparti-

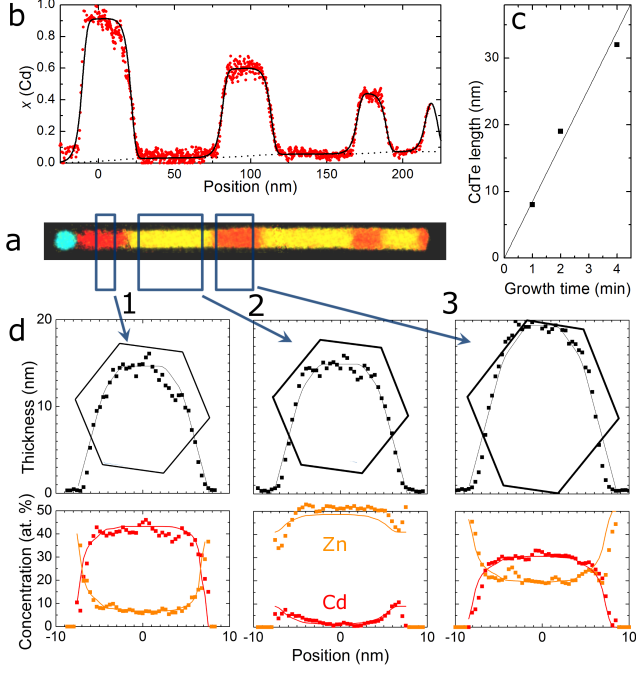


FIG. 3. Sample R: (a) EDX map (cyan: Au; yellow: Zn; red: Cd); (b) axial profile of Cd and fit (solid line) using the baseline shown by the dotted lines and elemental contributions using the same interface profile $\tau = 3.0$ nm, $\sigma = 2.0$ nm, and different values of length d ; (c) interface distance d as a function of the CdTe pulse length; the uncapped insertion is omitted; (d) radial profiles (total, Cd in red, Zn in orange) across the three rectangles shown in (a), and fit using the hexagonal cross-sections as indicated (the inner line indicates the boundary between the core and the multishell area; the internal boundaries of the multishell are not shown).

cle, $J_s \pi D_{NP}^2 / 4 \cos \alpha$ (the quasi-full sphere intercepts the total flux $J_s / \cos \alpha$ and not only its normal component J_s), and (2) the flux to the NW sidewalls, $J_s \tan \alpha$, integrated over the NW diameter and the diffusion length λ , $J_s \tan \alpha D_{NW} \lambda$. Their contribution to the growth rate of the NW of cross section area $\pi D_{NW}^2 / 4$ is thus

$$V_{NP}^{in} = \frac{J_s}{\cos \alpha} \frac{D_{NP}^2}{D_{NW}^2}, \quad V_{SW}^{in} = \frac{J_s \tan \alpha}{\pi} \frac{4\lambda}{D_{NW}}, \quad (2)$$

respectively. We neglect the contribution of the flux reflected or re-emitted from the substrate [22].

We now estimate the effect of the two negative contributions, evaporation from the nanoparticle and sublimation of CdTe adatoms from the sidewalls, to finally propose a global balance.

Cadmium is a volatile species: the vapor pressure above Cd at 350°C is $p_{Cd}^0 = 40$ Pa (compared to 2 Pa for Zn and 0.4 Pa for Te₂). The flux evaporating from a unit surface area is [23] $k_e p_{Cd} / \sqrt{2\pi M k_B T}$ with M the mass of a Cd atom (112 g for N_A atoms, with N_A the Avogadro constant), k_B the Boltzmann constant, T the

temperature, and k_e a factor representing barrier effects (in principle smaller than 1 but often omitted). In the case of a quasi-full sphere, this flux is integrated over the surface area, πD_{NP}^2 , and it reduces the growth rate of the NW of cross section area $\pi D_{NW}^2 / 4$ by a volume $a_0^3 / 4$ per Cd atom, where $a_0 = 0.648$ nm is the CdTe lattice constant. The final reduction of the growth rate is thus $V_{NP}^{out} = \frac{k_e p_{Cd}}{\sqrt{2\pi M k_B T}} a_0^3 \frac{D_{NP}^2}{D_{NW}^2}$. With $p_{Cd}^0 = 40$ Pa at 350°C, $\frac{p_{Cd}}{\sqrt{2\pi M k_B T}} a_0^3 \approx 0.3$ mm s⁻¹ (millimeter per second). This illustrates the benefit of a gold catalyst, which will reduce the Cd vapor pressure to $p_{Cd} = a p_{Cd}^0$ with an activity a much smaller than the Cd concentration c , and small enough to limit the evaporation of Cd to reasonable values: low values indeed were reported [24, 25] for the activity of Cd in gold at low concentration (8 to 10%), as low as 10⁻⁵ for 8% Cd in gold wires [25]. With such values, the loss of material due to the evaporation is reasonable, but not negligible. The temperature and concentration dependence is discussed in the supplementary material [26]: a reasonable extrapolation in the frame of the regular solution model is

$$p_{Cd}(c, T) = 3.3 \times 10^{10} c \times \exp \left[- \left(12100 + 7800 \frac{(1-c)^2}{1+0.27c} \right) \frac{1}{T} \right]. \quad (3)$$

That means that at 350°C, the equilibrium between our impinging flux and the evaporation of Cd in the nanoparticle is realized at 2% Cd; the equilibrium temperature rises above 400°C at 1% Cd. If the Cd concentration c stays around these values, we can neglect its influence on the value of the activation energy in Eq. 3. Actually the order of magnitude of c can be obtained if we assume that all the Cd contained in the exponential tail of length τ describing the interface (Eq. 1) is due to the reservoir effect in the gold nanoparticle. Distributing the Cd content of a cylinder of CdTe of height $\tau = 1.6$ nm and diameter $d_{NW} = 7.5$ nm, into a gold sphere of diameter $d_{NP} = 13$ nm (diameters measured on the TEM image) results in a concentration equal to 1.5% (a similar value, 2%, is calculated for the NW studied by EDX in Fig. 1). This is well below the concentration allowing the formation of Cd-Au compounds. Note that this is an average concentration; it gives no information about the distribution: uniform, or with an axial gradient, or a radial one, or even limited to the surface.

The sublimation of CdTe in the same temperature range is significant. In addition to several reports on the Cd and Te vapor pressure above CdTe, the sublimation rate from the (001) surface was measured by RHEED oscillations [27–29] together with the growth rate. The sublimation rate is [16] (in (001) ML s⁻¹): $V_{sub} = 3.1 \times 10^{-13} \exp(-21600/T)$, with an activation energy equal to 1.86 eV. This is close to the activation energy of vapor pressure measured above CdTe [30], $p_{Cd} p_{Te}^{\frac{1}{2}} \sim \exp(-33200/T)$, hence $p_{Cd} \sim \exp(-22100/T)$ under

congruent sublimation. Although the sublimation rate is expected to depend on the orientation of the surface (its anisotropy gives rise to the Wulff construction of the shape of a sublimating crystal), we will take the (001) rate as a first estimate of the sublimation from the NW sidewalls. It is worth at this point to remind the interpretation of the growth rate, which is smaller than the incident flux (incorporation less than unity): the difference involves two contributions, the sublimation, and the desorption of the adatoms which do not reach a nucleation center. In the case of 2D growth, nucleation centers are steps or stable nuclei (larger than the critical size). In the classical Burton-Cabrera-Frank analysis, which was applied to CdTe [31, 32], the flux of adatoms towards the steps is proportional to $(F - V_{sub})\lambda$, where F is the incident flux and V_{sub} the desorption rate, and the effective diffusion length λ takes into account the true diffusion length x_s (desorption) and the average distance between nucleation centers l_s (incorporation): $\lambda = \frac{x_s}{l_s} \tanh \frac{l_s}{x_s}$. In the case of a NW sidewall, the gold nanoparticle forms another trap, and if its efficiency is similar to that of the steps, it receives the same adatom flux $(F - V_{sub})\lambda$. As a result, the sublimation makes the flux smaller, through the factor $(F - V_{sub})$ instead of F . F itself is quite small if the flux-NW angle is small, and the lateral growth makes λ smaller either by the propagation of steps formed at the NW-substrate interface [33] or by the formation of critical nuclei on the sidewalls as in 2D growth [31, 32].

The contribution to the NW growth - positive if the diffusion takes place from the sidewall to the nanoparticle, or negative if from the nanoparticle to the sidewalls - is thus

$$(V_{SW}^{in} - V_{SW}^{out}) = \left(\frac{J_s \tan \alpha}{\pi} - V_{sub} \right) 4\lambda / D_{NW}. \quad (4)$$

With the present growth conditions ($J_s=0.5 \text{ ML s}^{-1}$ and $\tan \alpha=0.21$), the impinging flux is fully compensated by the sublimation around 350°C .

Finally, we should calculate the concentration c in the nanoparticle by writing the equilibrium between:

- the sum of the four previous contributions, $V_{NP}^{in} - V_{NP}^{out} + V_{SW}^{in} - V_{SW}^{out}$, where the first two terms result from the direct flux to the nanoparticle and the evaporation from the nanoparticle, and the last two terms are the contribution of the diffusion between the sidewalls and the nanoparticle.
- the nucleation at the NW tip. In the case of the self-catalyzed growth of GaAs NWs, the knowledge about the NW-nanodroplet interface is good enough, that classical nucleation theory can be fully developed and applied to calculate the nucleation rate as a function of the droplet composition [23]. It features a fast increase as a function of the difference of chemical potential - *i.e.*, as a function of the logarithm of the activity of As in the Ga droplet. We will use a crude approximation, by assuming

that the nucleation rate is zero below a threshold c_0 (which reflects the equilibrium concentration and the effect of the nucleation barrier) and then rises linearly with c . We ignore the stochastic nature of the nucleation [34] since we calculate an average growth rate.

The result is shown in Fig. 4b, where we plot the growth rate of ZnTe and CdTe segments in sample T and a similar sample grown at lower temperatures, as a function of temperature. For ZnTe we show only the segments at high growth rate, which are associated with quasi-full-sphere nanoparticles [15], and the fitting parameter is the diffusion length along the NW sidewalls. A good fit is obtained by assuming an activation energy 0.95 eV. A slow increase of the diffusion length with temperature was already noted [15] in association with a smaller tapering. For CdTe we keep the same geometrical parameters and diffusion length value, correct for the different angle of incidence, and we add the sublimation of CdTe and the evaporation of Cd from the gold nanoparticle, taken from the literature as discussed previously.

V. DISCUSSION

A. Growth rates

The four contributions to the growth rate are detailed in Fig. 4c. At low temperature, the only significant contribution is the direct flux to the nanoparticle. As the temperature increases, the diffusion length also increases and so does the contribution from the flux to the sidewall. However, this positive flux is rapidly compensated by the evaporation from the nanoparticle. In this temperature range, the flux is positive from the NW sidewalls to the nanoparticle. At higher temperature, the sublimation from the NW sidewalls becomes significant, so that the adatom density decreases (blocking the formation of lateral dots) and finally the flux is reversed, the Cd concentration in the nanoparticle goes down, and the axial growth is stopped. It appears that the evaporation of Cd from the gold nanoparticle, the small angle of incidence on the sidewalls and the sublimation of CdTe from the sidewalls conspire to achieve a low growth rate, a low concentration of Cd in the nanoparticle (resulting in sharp interfaces, much sharper than reported in earlier studies [35] realized in the VLS mode with Au-Ga liquid droplets at 450°C), and a low adatom density on the sidewalls (resulting in a weak lateral growth, as confirmed in the next subsection).

Other reports on the growth of CdTe NWs by MBE [13, 14] mention higher values of flux (larger values of the beam equivalent pressure on each of a Cd and a Te cells, than that from a single CdTe cell in our case). Additionally, the angle of incidence to the NW may be [14], or is on purpose [13], larger than ours. The temperature dependance of each of the four contributions, calculated

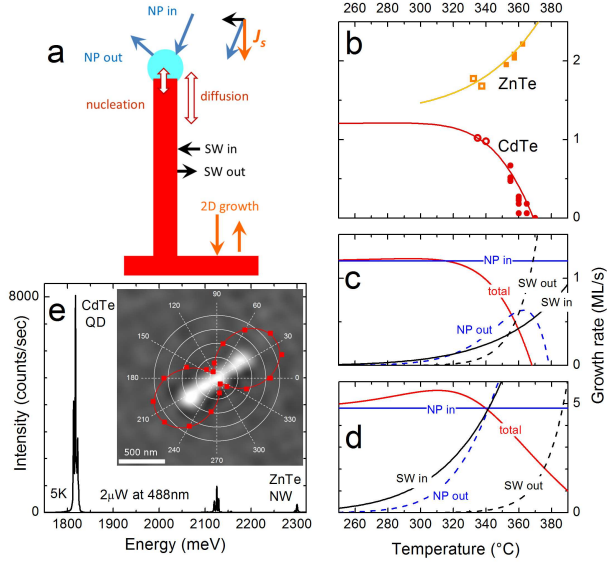


FIG. 4. (a) Scheme of the different contributions to the growth of the NW; the role of the different components of the incident flux (top right) is identified by their color (orange: normal component J_s contributing to the 2D growth and calibrated through RHEED oscillations; black: component $J_s \tan \alpha$ normal to the NW axis impinging the NW sidewalls; blue: total flux of intensity $J_s / \cos \alpha$) (b) growth rate of the ZnTe and CdTe segments of sample T (solid symbols) and another sample (open symbols), as a function of temperature. The normal incident flux measured on test (001) 2D layers is the same for both, 0.5 ML s^{-1} , with $\tan \alpha = 0.21$ for CdTe and 0.48 for ZnTe; the same unit is used for the growth rate of CdTe and ZnTe in the NW; (c) the four components entering the CdTe growth rate as calculated for the conditions in (b); (d) the four components for a higher flux (2 ML s^{-1}) and an oblique incidence ($\tan \alpha = 1$); (e) photoluminescence spectrum and (inset) polarization diagram superimposed on the image of the NW.

using the present model and for such conditions, is shown in Fig. 4d. The result is a higher growth rate at 350°C and a similar growth rate at 390°C . It is worth noting that the impact of the sublimation from the sidewalls is significantly decreased (it is now competing with a lateral flux with a higher intensity at relative incidence closer to the normal) so that the adatom density is expected to be larger than under our present growth conditions: in Fig. 1 each CdTe insertion contributes by less than one monolayer. This makes a sharp contrast with the thick shell (equivalent to 2 nm of pure CdTe) measured by EDX [19] on a sample we have grown previously using a high flux from a Cd cell with a large angle of incidence. Such a strong lateral growth is likely to give rise to the formation of additional quantum dots which complicate the photoluminescence spectra and indeed have been identified by cathodoluminescence [36].

B. Luminescence

As an example, Fig. 4e shows the photoluminescence spectrum of a CdTe-QD in ZnTe NW. The initial NW was grown at 375°C to reduce tapering, then the CdTe insertion was grown at 340°C as a compromise between a reasonably fast axial growth and a reasonably slow radial growth. The whole structure was capped with a (Zn,Mg)Te shell. The photoluminescence spectrum features three well separated bands which we associate (for increasing energies) to the long CdTe dot resulting from axial growth, to a parasitic CdTe inclusion resulting from lateral growth, and to ZnTe. Note that the polarization diagram shown in the inset is consistent with a light-hole exciton [10], while the polarization of the intermediate line (not shown) is oblique, suggesting that the principal axis of the insertion is not along the NW axis, and the polarization of ZnTe (not shown) is consistent with a heavy-hole exciton. Cathodoluminescence on the same NW (not shown) confirms that the three lines originate from well-separated areas along the NW.

C. Negative growth and nanoparticle shape

The unstable character of the CdTe segments at such temperatures (above 350°C) is also confirmed by the smaller length we systematically observed on the final, uncapped CdTe insertions in samples R and T. The CdTe segment is shorter while keeping the same diameter, an effect similar to what has been reported as "negative growth" upon annealing of GaAs NWs [37]. In the present case, it indicates that CdTe is re-dissolved into the gold nanoparticle as soon as the impinging flux has been stopped, creating a gradient of concentration, $\vec{\nabla}c$, directed on average from the interface towards the apex of the nanoparticle. This gradient drives the diffusion of Cd through the nanoparticle, with a flux $-D_{Cd} \frac{\nabla c}{\Omega}$ where D_{Cd} is the diffusion coefficient of Cd in Au, and Ω the atomic volume in gold ($= \frac{a_0^3}{4}$). The same gradient induces self-diffusion of gold in the opposite direction, with a flux $D_{Au} \frac{\nabla c}{\Omega}$. Diffusion in a substitutional solid solution is accompanied by the so-called vacancy drift, which is not balanced if the diffusion coefficients of the two atomic species are different. In the present case, they are indeed very different ($D_{Cd}/D_{Au} \approx 8$ at 1000K) [38] so that a number of vacancies approximately equal to the number of atoms dissolved is driven towards the interface, where they have to diffuse to the surface. As a result the nanoparticle tends to assume a bulb-like shape: this is indeed what we observe in Fig. 5 for a NW with the wurtzite structure. This is a manifestation of the Kirkendall effect, which has been known for years to create voids in alloys, and has been used recently to fabricate hollow nanostructures [39, 40]. Elongated shapes have been observed during redissolution of GaAs, InAs or SnO_2 NWs into gold nanoparticles upon heating [41–43].

We occasionally observe elongated nanoparticles, but the shape in Fig. 5 is more complex and well approximated by the shape of a pendant droplet [44–46], with a value of the characteristic parameter $\beta=0.037$. This is the signature of a quasi-uniform force field, directed along the axis, induced within the nanoparticle by the surface energy: in the pendant droplet [44–46], the force per unit volume is $\beta\frac{\gamma}{R^2}$, where R is the radius of curvature at the apex, γ is the energy per unit surface area; this force compensates the difference of weight per unit volume between the liquid in the droplet and the gas outside. The force corresponds to the gradient of the Laplace pressure which is uniform in a spherical droplet. In the context of nanowire growth, the equivalent of the Laplace pressure is the shift of the chemical potential within the catalyst droplet or nanoparticle (Gibbs-Thomson effect) [23]: in a spherical droplet, the shift is uniform, equal to $\frac{2\gamma}{R}\Omega$. The surface energy along the pendant-droplet shape results in a gradient of this chemical potential, equal to $\beta\frac{\gamma}{R^2}\Omega$, which decreases the Cd flux and increases the Au flux. The equilibrium shape is achieved when the vacancy drift vanishes, *i.e.*, when the Cd (or Cd and Te) and Au currents compensate each other. Within the regular solution model, the gradients of chemical potentials become $\nabla\mu_{Cd} = k_B T \frac{\nabla c}{c} - \beta\frac{\gamma}{R^2}\Omega$ and $\nabla\mu_{Au} = -k_B T \frac{\nabla c}{1-c} + \beta\frac{\gamma}{R^2}\Omega$, respectively. Balancing the diffusion flux of Cd and Au implies $D_{Cd}\nabla\mu_{Cd} = -D_{Au}\nabla\mu_{Au}$, hence $R\nabla c = \frac{D_{Cd}c + D_{Au}(1-c)}{D_{Cd} - D_{Au}}\beta\frac{1}{k_B T}\frac{\gamma\Omega}{R}$. With c a few %, $D_{Cd}/D_{Au} \approx 8$, $\Omega = 1.7 \times 10^{-2} \text{ nm}^3$, $\gamma=1.5 \text{ J m}^{-2}$ for gold [47], and $k_B T=50 \text{ meV}$, we obtain $R\nabla c \approx 10^{-3}$: the concentration drop between the interface and the apex is a (significant) fraction of the concentration estimated previously. This estimate is certainly oversimplified (we totally ignore the role of Te, and the actual flux distributions are more complex) but it shows that the orders of magnitude are realistic.

VI. SUMMARY

CdTe QDs have been grown in ZnTe NWs, with abrupt interfaces and a controlled aspect ratio, and reduced parasitic growth on the sidewalls. This is achieved in VSS

growth by MBE using a gold catalyst and a low flux of Cd and Te, quasi-parallel to the NW axis, at temperatures where a simple model shows that the sublimation of CdTe and the evaporation of Cd from the gold nanoparticle are significant. Similar concepts should apply to the growth of other systems, for instance NWs incorporating CdSe or HgTe. Very peculiar shapes of the gold nanoparticle are ascribed to the redissolution of CdTe under these specific conditions which - through the Kirkendall effect - favors the build up of a gradient of the chemical potential along the nanoparticle.

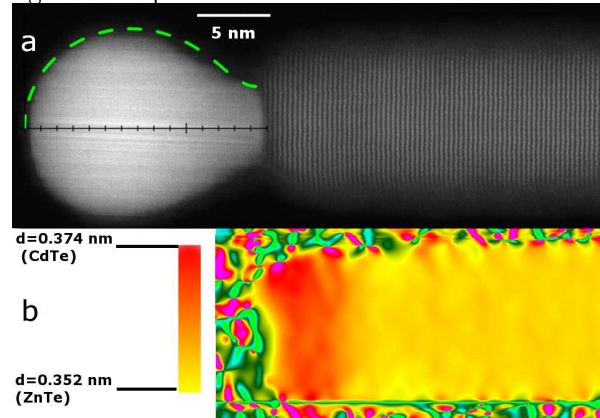


FIG. 5. (a) TEM image of the tip of a NW with the wurtzite structure, with a CdTe final segment as identified by the GPA (b). The green dashed line shows the shape calculated from the pendant droplet equation with $\beta = 0.037$. The color code is yellow for ZnTe (interplane distance 0.352 nm) and red for CdTe (interplane distance 0.374 nm).

ACKNOWLEDGMENTS

This work was performed in the joint CNRS-CEA group "Nanophysique & semiconducteurs", the team "Laboratory of Material Study by Advanced Microscopy", and the team "Materials, Radiations, Structure". We benefitted from the access to the Nano-characterization facility (PFNC) at CEA Minatec Grenoble. We acknowledge funding by the French National Research Agency (projects Magwires, ANR-11-BS10-013, COSMOS, ANR-12-JS10-0002, Espadon, ANR-15-CE24-0029 and labex LANEF ANR-10-LABX-51-01).

-
- [1] Yann-Michel Niquet and Dulce Camacho Mojica, Phys. Rev. B **77**, 115316 (2008).
 - [2] M. Zielinski, Phys. Rev. B **88**, 115424 (2013).
 - [3] Y. H. Huo, B. J. Witek, S. Kumar, J. R. Cardenas, J. X. Zhang, N. Akopian, R. Singh, E. Zallo, R. Grifone, D. Kriegner, R. Trotta, F. Ding, J. Stangl, V. Zwiller, G. Bester, A. Rastelli, O. G. Schmidt, Nature Phys. **10**, 46 (2014).
 - [4] C. Y. Wen, M. C. Reuter, J. Bruley, J. Tersoff, S. Kodambaka, E. A. Stach, and F. M. Ross, Science **326**, 1247

- (2009).
- [5] H. Cui, Y. Y. Lü, G. W. Yang, Y. M. Chen, and C. X. Wang, Nano Lett. **15**, 3640 (2015).
- [6] G. Priante, G. Patriarche, F. Oehler, F. Glas, and J.-C. Harmand, Nano Lett. **15**, 6036 (2015).
- [7] Jonas Johansson and Masoomeh Ghasemi, Phys. Rev. Materials **1**, 040401(R) (2017).
- [8] Kimberly A. Dick, Jessica B. Bolinsson, Mattias Borg, and Jonas Johansson, Nano Lett. **12**, 3200 (2012).

- [9] G. Priante, F. Glas, G. Patriarche, K. Pantzas, F. Oehler, and J.-C. Harmand, *Nano Lett.* **16**, 1917 (2016).
- [10] Mathieu Jeannin, Alberto Artioli, Pamela Rueda-Fonseca, Edith Bellet-Amalric, Kuntheak Kheng, Régis André, Serge Tatarenko, Joël Cibert, David Ferrand, and Gilles Nogues, *Phys. Rev. B* **96**, 035305 (2017).
- [11] S. Bounouar, M. Elouneq-Jamroz, M. den Hertog, C. Morchutt, E. Bellet-Amalric, R. André, C. Bougerol, Y. Genuist, J.-P. Poizat, S. Tatarenko, and K. Kheng, *Nano Lett.* **12**, 2977 (2012).
- [12] M. Szymura, P. Wojnar, L. Kłopotowski, J. Suffczynski, M. Goryca, T. Smolenski, P. Kossacki, W. Zaleszczyk, T. Wojciechowski, G. Karczewski, T. Wojtowicz, and J. Kossut, *Nano Lett.* **15**, 1972 (2015).
- [13] M. Kessel, J. Hajer, G. Karczewski, C. Schumacher, C. Brune, H. Buhmann and L. W. Molenkamp, *Phys. Rev. Materials* **1**, 023401 (2017).
- [14] P. Wojnar, J. Plachta, S. Kret, A. Kaleta, W. Zaleszczyk, M. Szymura, M. Wiater, L. T. Baczewski, A. Pietruczik, G. Karczewski, T. Wojtowicz, and J. Kossut, *Nanotechnology* **28**, 045207 (2017).
- [15] P. Rueda-Fonseca, M. Orrù, E. Bellet-Amalric, E. Robin, M. Den Hertog, Y. Genuist, R. André, S. Tatarenko, and J. Cibert, *J. Appl. Phys.* **119**, 164303 (2016).
- [16] A. Arnould and J. Cibert, *Appl. Phys. Lett.* **66**, 2397 (1995).
- [17] M. Lopez-Haro, P. Bayle-Guillemaud, N. Mollard, F. Saint-Antonin, C. Van Vilsteren, B. Freitag, and E. Robin, 18th International Microscopy Congress, Prague, 2014.
- [18] P. Rueda-Fonseca, E. Bellet-Amalric, R. Vigliaturo, M. den Hertog, Y. Genuist, R. André, E. Robin, A. Artioli, P. Stepanov, D. Ferrand, K. Kheng, S. Tatarenko, and J. Cibert, *Nano Lett.* **14**, 1877 (2014).
- [19] P. Rueda-Fonseca, E. Robin, E. Bellet-Amalric, M. Lopez-Haro, M. Den Hertog, Y. Genuist, R. André, A. Artioli, S. Tatarenko, D. Ferrand, and J. Cibert, *Nano Lett.* **16**, 1637 (2016).
- [20] M. Hÿtch, E. Snoeck and R. Kilaas, *Ultramicroscopy* **74**, 131 (1998).
- [21] J.-L. Rouvière and E. Sarigiannidou, *Ultramicroscopy* **106**, 1 (2005).
- [22] Mohammed Reda Ramdani, Jean Christophe Harmand, Frank Glas, Gilles Patriarche, and Laurent Travers, *Cryst. Growth Des.* **13**, 91 (2013).
- [23] Frank Glas, Mohammed Reda Ramdani, Gilles Patriarche, and Jean-Christophe Harmand, *Phys. Rev. B* **88**, 195304 (2013).
- [24] J. D. Filby and J. N. Pratt, *Trans. Faraday Soc.* **60**, 1934 (1964).
- [25] L. J. Bartha and W. A. Alexander, *Can. J. Chem.* **43**, 2319 (1965).
- [26] See Supplemental Material at [URL will be inserted by publisher] for the vapor pressure and diffusion of Cd in a gold nanoparticle.
- [27] J. M. Arias and G. Sullivan, *J. Vac. Sci. Technol. A* **5**, 3143 (1987).
- [28] A. Waag, Th. Behr, Th. Litz, B. Kuhn-Heinrich, D. Hommel, and G. Landwehr, *Mater. Sci. Eng. B* **16**, 103 (1993).
- [29] S. Tatarenko, B. Daudin, and D. Brun, *Appl. Phys. Lett.* **65**, 734 (1994).
- [30] Yang Jianrong, N.J. Silk, A. Watson, A.W. Bryant, and B.B. Argent, *Calphad* **19**, 399 (1995).
- [31] Philippe Peyla, Alberto Pimpinelli, Joël Cibert, and Serge Tatarenko, *J. Crystal Growth* **184/185**, 75 (1998).
- [32] Alberto Pimpinelli and Philippe Peyla, *J. Crystal Growth* **183**, 311 (1998).
- [33] Sergey N. Filimonov and Yuri Yu. Hervieu, *J. Cryst. Growth* **427**, 60 (2015).
- [34] Frank Glas and Vladimir G. Dubrovskii, *Phys. Rev. Materials* **1**, 036003 (2017).
- [35] P. Dłuzewski, E. Janik, S. Kret, W. Zaleszczyk, D. Tang, G. Karczewski, and T. Wojtowicz, *J. Microscopy* **237**, 337 (2010).
- [36] P. Wojnar, J. Plachta, W. Zaleszczyk, S. Kret, Ana M. Sanchez, R. Rudniewski, K. Raczkowska, M. Szymura, G. Karczewski, L. T. Baczewski, A. Pietruczik, T. Wojtowicz, and J. Kossut, *Nanoscale* **8**, 5720 (2016).
- [37] V. G. Dubrovskii, N. V. Sibirev, G. E. Cirlin, A. D. Bouravleuv, Yu. B. Samsonenko, D. L. Dheeraj, H. L. Zhou, C. Sartel, J. C. Harmand, G. Patriarche, and F. Glas, *Phys. Rev. B* **80**, 205305 (2009).
- [38] D. Decroupet and G. Demortier, *Nuclear Inst. Methods in Phys. B* **49**, 501 (1990).
- [39] Edgar González, Jordi Arbiol, and Víctor F. Puntes, *Science* **334**, 1377 (2011).
- [40] A.M. Gusak and K.N. Tu, *Acta Materialia* **57**, 3367 (2009).
- [41] Ann I. Persson, Magnus W. Larsson, Stig Stenström, B. Jonas Ohlsson, Lars Samuelson, and L. Reine Wallenberg, *Nature Mat.* **3**, 677 (2004).
- [42] R. S. Pennington, J. R. Jinschek, J. B. Wagner, C. B. Boothroyd, and R. E. Dunin-Borkowski *J. Phys.: Conference Series* **209**, 012013 (2010).
- [43] Bethany M. Hudak, Yao-Jen Chang, Lei Yu, Guohua Li, Danielle N. Edwards and Beth S. Guiton, *ACS Nano* **8**, 5441 (2014).
- [44] Y. Rotenberg, L. Boruvka, and A.W. Neumann, *J. Colloid Interface Sci.* **93**, 169 (1983).
- [45] F.K Hansen, and G. Rødsrud, *J. Colloid Interface Sci.* **141**, 1 (1991).
- [46] P.-M. Gassin, PhD thesis, Lyon 2013, <http://tel.archives-ouvertes.fr/docs/00/85/22/94/PDF/TheseGASSI>
- [47] L. Vitos, A.V. Ruban, H.L. Skriver and J. Kollár, *Surf. Sci.* **411**, 186 (1998).